



The Fast Radio Burst-emitting Magnetar SGR 1935+2154—Proper Motion and Variability from Long-term Hubble Space Telescope Monitoring

J. D. Lyman¹ , A. J. Levan^{1,2} , K. Wiersema^{1,3,4} , C. Kouveliotou^{5,6} , A. A. Chrimes² , and A. S. Fruchter⁷ ¹Department of Physics, University of Warwick, Coventry, CV4 7AL, UK²Department of Astrophysics/IMAPP, Radboud University Nijmegen, P.O. Box 9010, 6500 GL Nijmegen, The Netherlands³Physics Department, Lancaster University, Lancaster, LA1 4YB, UK⁴School of Physics and Astronomy, University of Leicester, University Road, Leicester, LE1 7RH, UK⁵Department of Physics, The George Washington University, Corcoran Hall, 725 21st Street NW, Washington, DC 20052, USA⁶GWU/Astronomy, Physics and Statistics Institute of Sciences (APSI), USA⁷Space Telescope Science Institute, 3700 San Martin Drive, Baltimore, MD 21218, USA

Received 2021 October 25; revised 2021 December 2; accepted 2021 December 10; published 2022 February 17

Abstract

We present deep Hubble Space Telescope (HST) near-infrared (NIR) observations of the magnetar SGR 1935+2154 from 2021 June, approximately 6 yr after the first HST observations, a year after the discovery of fast-radio-burst-like emission from the source, and in a period of exceptional high-frequency activity. Although not directly taken during a bursting period the counterpart is a factor of ~ 1.5 – 2.5 brighter than seen at previous epochs with F140W(AB) = 24.65 ± 0.02 mag. We do not detect significant variations of the NIR counterpart within the course of any one orbit (i.e., on minutes to hour timescales), and contemporaneous X-ray observations show SGR 1935+2154 to be at the quiescent level. With a time baseline of 6 yr from the first identification of the counterpart we place stringent limits on the proper motion (PM) of the source, with a measured PM of $\mu = 3.1 \pm 1.5$ mas yr⁻¹. The direction of PM indicates an origin of SGR 1935+2154 very close to the geometric center of SNR G57.2+08, further strengthening their association. At an adopted distance of 6.6 ± 0.7 kpc, the corresponding tangential space velocity is $v_T = 97 \pm 48$ km s⁻¹ (corrected for differential Galactic rotation and peculiar solar motion), although its formal statistical determination may be compromised owing to few epochs of observation. The current velocity estimate places it at the low end of the kick distribution for pulsars, and makes it among the lowest known magnetar kicks. When collating the few-magnetar kick constraints available, we find full consistency between the magnetar kick distribution and the much larger pulsar kick sample.

Unified Astronomy Thesaurus concepts: Magnetars (992); Soft gamma-ray repeaters (1471); Neutron stars (1108); Radio transient sources (2008); Radio bursts (1339); Astrometry (80); Proper motions (1295)

1. Introduction

Magnetars are a diverse set of neutron stars (NSs) with magnetic fields in excess of $B \sim 10^{14}$ G (e.g., Duncan & Thompson 1992; Kouveliotou et al. 1998; Kaspi & Beloborodov 2017). In the Milky Way they manifest predominantly as soft-gamma repeaters (SGRs) and anomalous X-ray pulsars, although some rotational powered pulsars have also exhibited magnetar-like behavior (Gavriil et al. 2008). The Galactic population currently numbers >30 objects (Olausen & Kaspi 2014), the majority of which have spin periods of 1–10 s, and characteristic spin-down ages of 100–10,000 yr.

Magnetars provide an ideal test-bed for several areas of extreme astrophysics since they probe matter under the effect of extreme density, magnetic field strength, and gravity. In recent years, magnetars have been of particular interest for their role as central engines in transient extragalactic events, including some of the most energetic events we know of. The creation and subsequent spin-down of new magnetars has been invoked to explain superluminous supernovae (e.g., Kasen & Bildsten 2010; Woosley 2010; Inerra et al. 2013; Dessart 2019), and both long- and short-duration gamma-ray bursts (GRBs; e.g., Usov 1992; Zhang & Mészáros 2001; Beniamini et al. 2017). In this scenario, the early

millisecond spin periods and very strong fields lead to rapid spin-down, which can power either GRB-like emission for spin-down times of seconds, or luminous supernovae for spin-down times of weeks (Metzger et al. 2015, 2018).

Magnetars are also prime candidates as the origins of fast radio bursts (FRBs). Although it now appears likely that there are at least two classes of such events (Pleunis et al. 2021), multiple lines of evidence imply that at least some may be created by magnetars. This includes the strong measures of Faraday rotation in repeating FRBs that imply strong magnetic fields, the location of some well-localized FRBs in star-forming regions similar to those that host supernovae and GRBs (Heintz et al. 2020; Bochenek et al. 2021), and the galactocentric offset distribution of FRBs being consistent to that of Galactic NS stars (Bhandari et al. 2022). Recently, detailed environmental analysis by Chrimes et al. (2021), when considering the Milky Way as an FRB host, has shown good consistency between distributions of diagnostics for FRBs environments—such as their location in the light distribution of their host (following Fruchter et al. 2006)—and what the equivalent distributions would be for Milky Way magnetars from an extragalactic vantage point.

However, arguably the strongest evidence for an FRB-magnetar link arises from the detection of FRB-like bursts from the Galactic magnetar SGR 1935+2154 (Bochenek et al. 2020; CHIME/FRB Collaboration et al. 2020; Kirsten et al. 2021). These Galactic bursts had similar signatures and durations to extragalactic FRBs, however, when compared the subset of



Original content from this work may be used under the terms of the [Creative Commons Attribution 4.0 licence](https://creativecommons.org/licenses/by/4.0/). Any further distribution of this work must maintain attribution to the author(s) and the title of the work, journal citation and DOI.

extragalactic FRBs that have been localized to host galaxies, they appear much less luminous (e.g., Nimmo et al. 2021). The luminosity of the SGR 1935+2154 bursts means that they would not be detectable in external galaxies, and so the lack of similar luminosity bursts in the extragalactic sample is not surprising. Indeed, the presence of these low-luminosity bursts appears to indicate we are missing the full luminosity distribution of FRBs when accounting only for the extragalactic population. During active episodes, some magnetars emit multiple X-ray bursts (sometimes called burst storms or burst forests) with a very broad range of luminosities. In even rarer cases, magnetars emit giant flares (e.g., Mazets et al. 1979); only three have been thus far observed in our galaxy. However, several more have been recently identified to originate from external galaxies (Burns et al. 2021), with properties akin to a short GRB (Hurley et al. 2005; Palmer et al. 2005). Similar behavior occurring in the radio might yield detectable repeating FRBs from extragalactic magnetars.

SGR 1935+2154 is one of the most active magnetars in the Galaxy and the possibilities it now offers to observe an FRB-emitting system in intricate detail has compounded its astrophysical interest. It is spatially coincident with the supernova remnant SNR G57.2+08 (Gaensler 2014), which is typically inferred to be the result of the magnetar-producing supernova (Kothes et al. 2018; Zhou et al. 2020; dos Anjos et al. 2021). The supernova itself, based on a study of the remnant, does not appear to be extraordinary by core-collapse standards (Zhou et al. 2020), hinting that magnetar production in the deaths of massive stars may be more widespread than initially thought. This scenario is appealing given the current tension for *normal* core-collapse supernovae between the theoretical expectations of purely radioactively powered explosions (Ertl et al. 2020; Woosley et al. 2021) and observations (Sollerman et al. 2022).

SGR 1935+2154 underwent a new period of increased activity throughout mid-2021, triggering multiple high-energy missions, including Fermi (Lesage et al. 2021), INTEGRAL (Mereghetti & IBAS localization Team 2021), GECAM (Xiao et al. 2021), Neil Gehrels Swift Observatory (Palmer & Swift Team 2021), Konus-Wind (Ridnaia et al. 2021), and Calet (Nakahira et al. 2021), although as yet no FRB-like emission has been reported during this time, nor indeed any detectable radio detection (Singh & Roy 2021).

Here we present Hubble Space Telescope (HST) near-infrared (NIR) observations of SGR 1935+2154 obtained during its recent period of enhanced activity. Our observations confirm the detection of the counterpart with good statistics 6 yr after its previous detection. We discuss the implications of this new detection for the origin of the NIR emission. Additionally, our observations place constraints on the proper motion (PM) of SGR 1935+2154, thereby, constraining the kick imparted to the magnetar at birth.

1.1. Distance to SGR 1935+2154

Much of our analysis of SGR 1935+2154 imposes a need to know the distance to the object. This distance has been somewhat contentious, usually being measured by proxy of the distance to SNR G57.2+08 and using several different means, often with discrepant results. Estimates range anywhere from ~ 6 to 14 kpc (e.g., Park et al. 2013; Pavlovic et al. 2014; Surnis et al. 2016; Kothes et al. 2018; Zhong et al. 2020; Zhou et al. 2020). For our purposes we will adopt the distance of 6.6 ± 0.7 kpc determined in a recent study by Zhou et al.

Table 1
HST WFC3/IR Observations of SGR 1935+2154

Epoch	MJD (days)	PA _{V3} (degrees)	Exp. Time (seconds)	Filter
(1)	(2)	(3)	(4)	(5)
2015.2	57083.976129	115.218903	2396.929	F140W
2015.6	57252.355994	295.220612	2396.929	F140W
2016.4	57539.962668	25.218519	2396.929	F140W
2021.4	59366.721959	25.218519	2396.929	F140W

Note. (1) The name of the observation epoch as referred to in the text. (2) Modified Julian Date at the midpoint of epoch observation. (3) The position angle of the V3 axis of HST for the first exposure—this is closely related to the roll angle. (4) Total exposure time of observation. Epochs 2015.2, 2015.6, and 2016.4 have been previously presented in Levan et al. (2018).

(2020) of molecular clouds impacted by SNR G57.2+08. The motivation for favoring a lower distance in part comes from an SNR-independent distance estimate to SGR 1935+2154 from the detection of an X-ray dust scattering ring by Mereghetti et al. (2020), who estimate a distance of $4.4^{+2.8}_{-1.3}$ kpc. Even more recently, Bailes et al. (2021) estimated a distance to SGR 1935+2154, based on line-of-sight measures such as column density and extinction, of 1.5–6.5 kpc—again consistent with the lower estimates of the SNR. Where appropriate, we also discuss the impact of distance on our results.

2. Observations and Data Reduction

New observations presented here were taken with HST Wide Field Camera 3 (WFC3)/IR in F140W on 2021 June 1 (Program 16505; PI: Levan), covering 4.65 arcmin^2 around SGR 1935+2154. Total observation time was 2497 s, split over four equal exposures with sub-pixel dithering. This latest observation will be referred to as Epoch 2021.4 and it follows observations from three earlier epochs of similar observations of SGR 1935+2154, which were first presented in Levan et al. (2018), to be referred to as Epochs 2015.2, 2015.6, and 2016.4. Since accurate alignment with the previous epochs was desired for the purpose of astrometry, the same observing parameters, including roll angles of the telescope kept in 90° steps, were used. In particular, Epochs 2016.4 and 2021.4 share close to an exact observing repeat, separated by 5 yr. Observation details of the epochs are given in Table 1.

For each epoch, the four individual `_flt.fits` were drizzle-combined (Fruchter & Hook 2002) using AstroDrizzle within DrizzlePac v3.1.8.⁸ We fixed the final pixel scale to 65 mas, i.e., roughly halving the native pixel scale. All mentions of pixels throughout are on this pixel scale. The rotation of the drizzled images were set to align with the equatorial coordinates system, such that ΔX and ΔY in image pixel coordinates directly translate to $\Delta\alpha$ and $\Delta\delta$.

3. Methods

Throughout we have implicitly assumed the source is point-like in our HST images, any deviation from this would further increase photometric and astrometric uncertainties.

⁸ <https://www.stsci.edu/scientific-community/software/drizzlepac.html>

3.1. Photometry

Photometry was measured using DOLPHOT V2.0 (Dolphin 2000)⁹, using the WFC3/IR package and using updated point-spread function (PSF) cores from Anderson (2016). Although drizzled images suffer a number of effects that can compromise their use for photometry, we did use the drizzled image for each epoch as an input reference image for DOLPHOT, as this is used only to initially find sources. For each epoch, the sources are then photometered on the individual (natively sampled) `_flt.fits` exposures using empirical PSFs, for accurate photometry and astrometry. The final source position and photometric measurements are then determined from a combination of the individual `_flt.fits` measurements. Using the known position of SGR 1935+2154 (Levan et al. 2018) we recover the counterpart in each epoch—although faint, it is well detected in each epoch, with $\log_{10}(\text{Counts}) \sim 3.7\text{--}4.1$. DOLPHOT natively produces photometry in the VEGAMAG system. To convert to ABMAG, which we will use throughout, we make use of `stsynphot`¹⁰ v1.1.0 to compute the offset between these two systems in the F140W filter, finding the additive correction to be 1.0973 mag, which we add to each of the output magnitudes from DOLPHOT.

During the course of manual inspection of the frames, it was noticed that the first exposure of Epoch 2015.6 is affected by what appears to be a cosmic ray. This object is automatically masked by DOLPHOT and means the photometry is significantly compromised for this exposure at the level of offer only a weak detection (SNR ~ 2 see ~ 10 for other exposure in this epoch). Despite the poor constraints, we opt to use this measurement in subsequent analyses, including in the calculation of the final combined photometry for that epoch, but we note in the text wherever this is not the case.

3.2. Astrometry

With a significant baseline of observations, spanning more than 6 yr, we can take advantage of the stability of HST to perform accurate astrometry of SGR 1935+2154 in order to place constraints on the PM of the source. As we have no line-of-sight constraints, any discussion of PM ($=\mu$) relates to tangential—i.e., plane-of-sky—motion only.

For our astrometric work, we significantly cut the original DOLPHOT photometry tables, per epoch, for quality. Any source that was not given a *bright star* type classification by DOLPHOT was thrown out. This removes some faint stars, as well as any extended objects. Next we set a crowding limit of 0.7 mag, i.e., we remove any stars for which their magnitude brightens by more than 0.7 mag if neighboring stars are not accounted for. This removes a lot of spurious sources as well as preferentially leaving isolated sources. We then cut any object for which DOLPHOT found a zero or negative flux (spurious sources) and finally drop the faintest 10% of sources that survived previous cuts. This left $\sim 15,000$ surviving sources per epoch, and a manual inspection of the source catalogs indicated a very high level of commonality of sources between epochs.

The precision of the Gaia astrometric solution now offers the opportunity for absolute astrometry to be performed with HST imaging at a comparable level to that found with differential astrometry through tying relative astrometric coordinate systems

to the Gaia reference frame. The reader is referred to Bedin & Fontanive (2018), hereafter BF18, for a full and thorough pedagogical explanation for the method, which will comparatively only be summarized for our particular use case here. Where appropriate, we follow their notation described in their Section 3.3. (Note that we do not foresee any chance of significant parallax measurements of our source, given its expected distance, and so we do not apply any corrections to compute this value absolutely, see, e.g., Bedin & Fontanive 2020.)

First, TOPCAT¹¹ was used to extract a cone of sources in the Gaia Early Data Release 3 (EDR3; Gaia Collaboration et al. 2021). From these sources we exclude any that do not have at least a five-parameter astrometric solution computed—positions and PM in equatorial coordinates as well as a parallax (and pseudo-color for the six-parameter solutions), and then remove any for which the renormalized unit weight error (RUWE; Lindegren et al. 2021) is greater than 1.2. This cut on RUWE effectively removes those with poor astrometric solutions and is even stricter than that done in Gaia EDR3 catalog validation (Fabricius et al. 2021), as we strongly prioritize quality rather than quantity of the tie points for our astrometry. We used the crude World Coordinate System (WCS) information pre-populated in the HST data to convert the position of surviving Gaia sources into approximate (X, Y) pixel coordinates for each epoch, simply for the purpose of doing a very rough and generous first cross match with a subset of bright sources in the HST images. This provided us with a means to automatically determine a matched list of Gaia sources with the accurate (X, Y) coordinates of their HST-detected counterparts. The equatorial Gaia coordinates were corrected for their PM in order to obtain their positions as they would have appeared at each of our HST epochs (e.g., see Equation (5) of BF18). Using Equation (3) of BF18, epoch-corrected Gaia equatorial coordinates were converted to those of a tangent plane with coordinates (ξ, η) . This plane is defined with a tangent point of (α_o, δ_o) , the values of which were simply chosen to be the reference coordinates of the WCS for each epoch’s image. These (ξ, η) coordinates of Gaia sources could then be further converted into (X, Y) pixel coordinates for each epoch, following Equation (1) of BF18, after an appropriate fitting of the coefficients.

Using the matched Gaia and HST source lists, we initially fitted for the linear coefficients of Equation (1) in BF18 using the Gaia (ξ, η) coordinates, and the HST (X, Y) coordinates in a weighted least-squares (Levenberg-Marquardt) manner using `lmfit` (Newville et al. 2014). From this initial fit we identified any matches with an offset larger than $P_{95\%}$ of the distribution to prevent outliers affecting the fitting, and removed those before repeating the fit to obtain our final fitted parameters. Practically, the exact choice of percentile rejection made little difference to results, so long as the few most discrepant sources, which were noticeably poorer than the overall distribution of offsets for some epochs, were removed for each fit. The nominal value of parameters and uncertainties from the final fits were determined by propagating Gaia astrometric uncertainties in position and PM onto the (ξ, η) coordinates, and repeating the fitting 2000 times with resampled realizations of these coordinates. The median and standard deviation of these results gave our results. For the linear parameters we also add in quadrature the median

⁹ <http://americano.dolphinim.com/dolphot/>

¹⁰ https://github.com/spacetelescope/stsynphot_refactor

¹¹ <http://www.star.bris.ac.uk/~mbt/topcat/>

Table 2
HST WFC3/IR Photometry of SGR 1935+2154

Epoch	MJD (days)	Data Set	m_{F140W} (AB mag)	$\sigma(m_{F140W})$ (AB mag)
(1)	(2)	(3)	(4)	(5)
2015.2	57083.964654	icst01htq	25.194	0.083
	57083.972304	icst01huq	25.271	0.085
	57083.979955	icst01hwq	25.274	0.087
	57083.987605	icst01hxq	25.073	0.071
	57083.976129	combined	25.199	0.041
2015.6	57252.344519	icst01htq	26.634	0.491
	57252.352169	icst01huq	25.440	0.101
	57252.359820	icst01hwq	25.707	0.104
	57252.367470	icst01hxq	25.501	0.094
	57252.355994	combined	25.625	0.058
2016.4	57539.929757	icst01htq	25.088	0.066
	57539.937408	icst01huq	25.083	0.066
	57539.945058	icst01hwq	25.195	0.075
	57539.995579	icst01hxq	25.051	0.065
	57539.962668	combined	25.103	0.034
2021.4	59366.710483	icst01htq	24.714	0.048
	59366.718134	icst01huq	24.725	0.048
	59366.725784	icst01hwq	24.608	0.048
	59366.733435	icst01hxq	24.545	0.045
	59366.721959	combined	24.652	0.024

Note. (1) The name of the observation epoch as referred to in the text. (2) MJD at midpoint of exposure. (3) The `_flt.fits` data set name of the exposure as retrieved from the HST archive—“combined” indicates the combined photometry for each epoch. (4) and (5) The AB magnitude and uncertainty of SGR 1935+2154.

statistical uncertainty on the fit into our uncertainty budget for these values.

For the Gaia–HST removed matches (i.e., those with offsets $> P_{95\%}$ after the initial fit), manual inspection did not reveal any strongly obvious reason for their larger offsets in terms of crowding, chip location, etc. The Gaia astrometric parameters from these sources were typically larger than the overall source matches, and could be indicative of incorrect and lack of treatment of the PM and parallax, respectively.

It is worth noting at this point that we would ideally wish to use solely quasi-stellar objects (QSOs) for our tie points—point-like sources with practically zero PM and parallax. In this case the differential movement of our tie points between epochs in the Gaia reference frame would not be a concern. However, owing to sky density of QSOs, and the Galactic location of SGR 1935+2154 in the plane, we have no such objects within our field of view.

4. Results

4.1. Photometry

Photometry of SGR 1935+2154, calculated as detailed in Section 3.1, is presented in Table 2 and shown in Figure 1. SGR 1935+2154 is significantly variable on timescales of years and has undergone a factor ~ 2.5 increase in brightness between Epochs 2015.6 and 2021.4. In addition to this, we investigated the possibility of variability on short (minutes) timescales. For this we determined p -value for the null hypothesis of no variability by modeling the magnitudes as a constant. The first three epochs, 2015.2, 2015.6, and 2016.4, provide $< 2\sigma$ rejection of this null

hypothesis (we trialed 2015.6 with and without the compromised first exposure), with 2021.4 rejecting at $p = 0.016$. Overall we find no strong evidence for short timescale variability of SGR 1935+2154 in current observations, with future observations—especially if the IR counterpart remains brighter, which allows for more precise photometry—needed to rule more conclusively.

4.2. Astrometry

Our final fitted parameters from the absolute astrometry, and associated fit statistics, are given in Table 3. The $\sigma(\Delta X)$ and $\sigma(\Delta Y)$ values, which give the typical spread of offsets between HST image source positions and transformed Gaia equatorial coordinates in the (X, Y) pixel coordinate system, are comparable or lower than that obtained from differential astrometry of HST frames.¹² First, we can conclude that the precision of the Gaia astrometric solution is not a limiting factor in our transformation, and that the move to an absolute reference frame is possible without sacrificing precision, e.g., differential astrometry. We further conclude that strict selection of tie points for absolute astrometry, as detailed in Section 3.2, and the ability to correct for the known PM of tie point sources, are significant aids in the accuracy of the fit results.

As a sanity check for our transformations and subsequent PM calculations, we compared results from our routine to calculate PMs from HST data with Gaia EDR3 PMs for the 50 brightest sources in a region at the center of the HST images that is covered by all four epochs. The results of this are shown in Figure 2, which highlights excellent agreement.

We used our absolute astrometry to perform a cross match of all sources similar in brightness ($23.5 < m_{F140W} < 24.5$ mag) to SGR 1935+2154—around 2700 sources per epoch. For this cross match we converted all (X, Y) coordinates of the sources into the Gaia Equatorial frame in (α, δ) using our fitted parameters, and then matched our sources in equatorial coordinates between epochs, allowing a generous matching radius of 75 mas (the reason for which will become apparent). The results of these cross matches are shown in the three subplots of Figure 3. What is immediately clear is the systematic shift in the offsets as the baseline of time between epochs increases. This indicates bulk motion of the field, and to determine the *peculiar* velocity of SGR 1935+2154 within this bulk motion, it must be accounted for. We surmised this to be a manifestation of differential Galactic rotation and thus sought to model its effect.

Sources at different sight lines and distances throughout the Galaxy will have a Galactic PM associated with them, which arises as a combination of their rotation in the Galaxy and the solar peculiar motion, each with respect to the local standard of rest (LSR). We follow largely the procedure in (Verbunt et al. 2017, Section 3.2), albeit with updated parameters. The velocity of the Sun with respect to the LSR is taken to be $(U, V, W) = (8.63 \pm 0.64, 4.76 \pm 0.49, 7.26 \pm 0.36)$ km s⁻¹ (Ding et al. 2019), with the components of motion being toward the Galactic center, along Galactic rotation, and perpendicular to the Galactic plane, respectively. We use a constant rotation velocity, $v_R = 220$ km s⁻¹ (IAU standard) for both the LSR and our field since all sight-line distances have Galactocentric distances outside the turnover to a flat rotation speed profile for the Milky Way

¹² See, for example, Levan et al. (2018). Our own differential astrometric exercises with these data using `spalpy` (Lyman 2021) for astrometric alignment provided comparable, but slightly larger, alignment residuals—this prompted us to concentrate solely on the absolute astrometry.

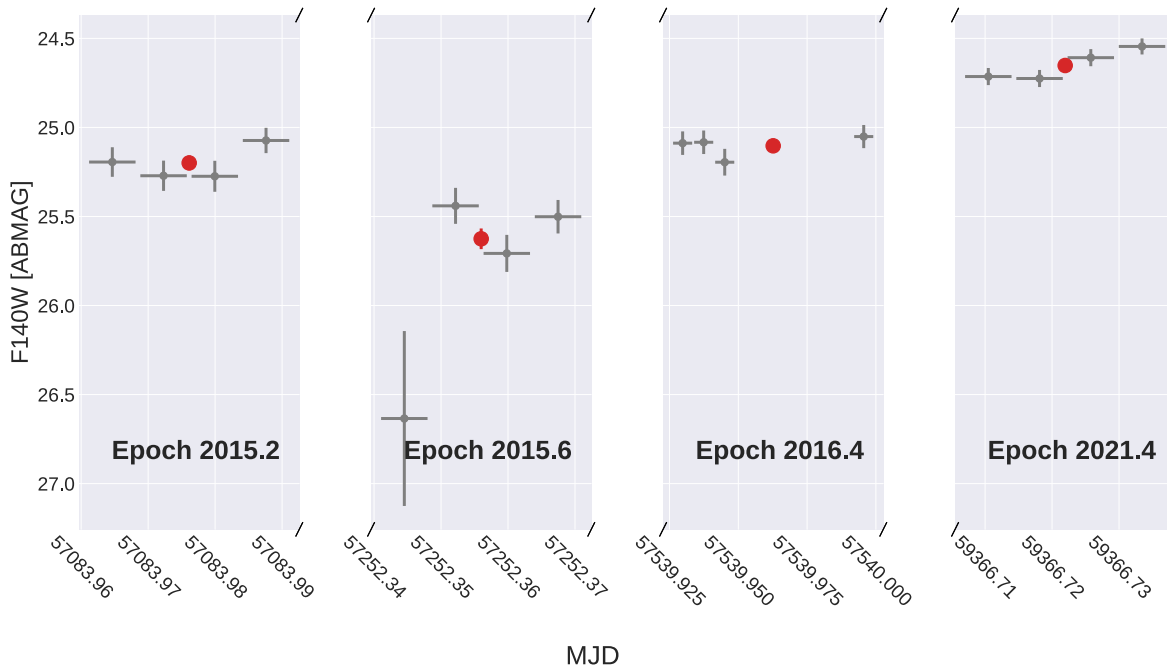


Figure 1. The HST WFC3/IR F140W light curve of SGR 1935+2154. Small gray points indicate photometry from individual `_flt.fits` data, larger, blue points indicate the combined photometry per epoch. The variability of SGR 1935+2154 on long timescales (note the broken abscissa axis) is apparent from the deviation of the blue points, although intra-epoch variability is less clear (see text). As discussed in the text, the errant measurement in the first exposure of Epoch 2015.6 was caused by a cosmic ray hit on top of the SGR 1935+2154 in the data.

(~ 3 kpc, e.g., Reid et al. 2014). Finally, we set the Sun’s Galactocentric distance as 8.122 ± 0.033 kpc (Gravity Collaboration et al. 2018). Models such as this have also been employed elsewhere in the pursuit of PM constraints for other similar objects (e.g., Dodson et al. 2003; Deller et al. 2012; Tendulkar et al. 2012).

The sight line to SGR 1935+2154 is dominated by the Perseus arm of the Milky Way, at a distance of ~ 8 kpc (Vallée 2008) and in Figure 3 we show vectors of bulk motion of the field due to differential Galactic rotation at this distance. The vectors, particularly for our longest baseline between epochs in the third subplot, quite accurately account for the shift in the peak of the distributions from the origin in these plots. With the model verified, we are therefore able to quantify the effect of Galactic motion on SGR 1935+2154 (for a given distance) and therefore, by removing this Galactic motion, we can derive its peculiar velocity—the quantity of interest to study the nature of its natal kick.

Following Section 1.1, we use 6.6 ± 0.7 kpc as our adopted distance to SGR 1935+2154. Accounting for uncertainties both in the model parameters (where given), as well as the distance, we derive a Galactic PM for SGR 1935+2154 of $(\mu_{\alpha^*, G}, \mu_{\delta, G}) = (-2.64 \pm 0.04, -5.20 \pm 0.04)$ mas yr $^{-1}$. The remaining motion of SGR 1935+2154 in our absolute frame is its peculiar motion with respect to its own LSR. In Figure 4, we show the position of SGR 1935+2154 in each epoch relative to the mean position across all four epochs: $(\bar{\alpha}_{\text{SGR}}, \bar{\delta}_{\text{SGR}}) = (293.73170336, 21.89657038)$ deg. A linear model was constructed and fitted in a weighted least-squares manner to the relative motion of SGR 1935+2154. For the offsets’ uncertainties, the positional uncertainty on the SGR 1935+2154 itself, the typical offset residuals after alignment to the Gaia frame (Table 3), and the uncertainty on the Galactic PM were all added in quadrature as sources of random statistical error.

Our fitting gave $(\mu_{\alpha^*}, \mu_{\delta}) = (-0.73 \pm 0.74, 3.03 \pm 1.55)$ mas yr $^{-1}$, i.e., a total PM of $\mu = 3.12 \pm 1.52$ mas yr $^{-1}$, or motion at the $\sim 2.1\sigma$ level of confidence. We note that our fitting procedure would ideally be performed on fully homoscedastic data consisting of a large number of data points. Unfortunately, we are limited to only four data points for our fitting (although noting each point are themselves effectively averages constructed from four independent measurements in the individual `_flt.fits` files), and as such the central-limit theorem is not in action—this makes translating the $\sim 2.1\sigma$ detection of motion to a formal probability more difficult. With these caveats in mind, we work with the above value for the PM of SGR 1935+2154 as the current best available constraints, and finally note even if we were to consider this a non-detection, given our low uncertainties, our discussions and conclusions remain unchanged. Figure 2 gives further credence that the fitting procedure produces results in line with those determined from a richer astrometric data set.

Since our corrections for Galactic motion are distance dependent the tangential space velocity in units of kilometers per second is not a simple function of assumed distance to SGR 1935+2154. In Figure 5, we show the results for a variety of assumed distances to SGR 1935+2154, and note that the overall change based on assumed distance is largely dwarfed by the astrometric uncertainty. Taking two example distance estimates at the lower and upper bounds from the literature— 6.6 ± 0.7 kpc (Zhou et al. 2020) and 12.5 ± 1.5 kpc (Kothés et al. 2018)—we obtain tangential space velocities of $\nu_T \sim 97 \pm 48$ and 140 ± 89 , km s $^{-1}$, respectively (note these values include the additional uncertainty contribution from the distance assumed).¹³

¹³ For the distance estimate of Kothés et al. (2018), other corresponding values are $(\mu_{\alpha^*, G}, \mu_{\delta, G}) = (-2.24 \pm 0.14, -4.22 \pm 0.28)$ mas yr $^{-1}$, $(\mu_{\alpha^*}, \mu_{\delta}) = (-1.11 \pm 0.75, 2.09 \pm 1.60)$ mas yr $^{-1}$, and $\mu = 2.36 \pm 1.48$ mas yr $^{-1}$.

Table 3Fitted Linear Coefficients and Fitting Statistics for Transformations between the (X, Y) Pixel Coordinate System of Each Epoch and a Tangent Plane (ξ, η) Defined in the Gaia EDR3 Reference Frame

Value	Epoch			
	2015.2 (2)	2015.6 (3)	2016.4 (4)	2021.4 (5)
Linear parameters				
\mathcal{A} [mas]	-65.0081 ± 0.0003	-65.0024 ± 0.0004	-65.0077 ± 0.0003	-65.0039 ± 0.0011
\mathcal{B} [mas]	0.0037 ± 0.0003	0.0010 ± 0.0005	0.0019 ± 0.0003	0.0036 ± 0.0010
\mathcal{C} [mas]	0.0040 ± 0.0003	0.0004 ± 0.0004	0.0018 ± 0.0003	0.0032 ± 0.0011
\mathcal{D} [mas]	65.0058 ± 0.0004	65.0012 ± 0.0005	65.0092 ± 0.0003	65.0038 ± 0.0011
\mathcal{X}_0 [pix]	1249.473 ± 0.003	1492.008 ± 0.004	1260.481 ± 0.003	1257.427 ± 0.009
\mathcal{Y}_0 [pix]	1092.708 ± 0.003	1174.197 ± 0.004	1331.946 ± 0.003	1331.024 ± 0.009
α_0 [deg]	293.72961531	293.73437466	293.7312987	293.7312413
δ_0 [deg]	21.89747904	21.89599149	21.8944872	21.8945040
Fitting statistics				
Initial Gaia–HST matches	128	125	118	117
Clipped matches	7	7	6	6
$\sigma(\Delta X)$ [pix]	0.025 ± 0.001	0.043 ± 0.001	0.027 ± 0.001	0.075 ± 0.006
$\sigma(\Delta Y)$ [pix]	0.031 ± 0.001	0.043 ± 0.001	0.027 ± 0.001	0.081 ± 0.008
Offset residual $P_{68\%}$ [mas]	2.6	4.1	2.8	5.2
Offset residual $P_{99\%}$ [mas]	4.8	7.5	4.2	10.7

Note. (1) The name of the value. Linear parameter definitions follow those of BF18; fitting statistics denote, respectively, the number of initial matches used to fit the linear transformation, the number of clipped matches before doing the final fit (i.e., those with offsets $> P_{95\%}$ after the initial fit), the standard deviation of the X and Y pixel offsets of matched sources, and their 68th and 99th percentile total offset residuals in milliarcsecond. (2)–(5) The value in the specific epoch’s fit.

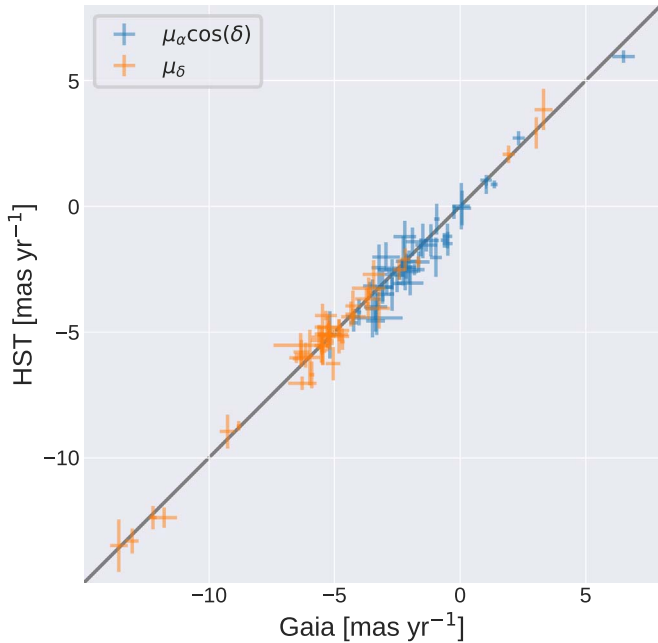


Figure 2. The PM constraints for 50 sources in the center of the HST field of view from our own HST calculations, and those of Gaia EDR3. We observe excellent agreement, with no evidence of a systematic shift in either coordinate at high or low absolute values.

5. Discussion

5.1. Photometric Evolution and Origin of NIR Emission

The most recent epoch of HST imaging at 2021.4 shows a factor of 1.5–2.5 brightness increase in SGR 1935+2154 over earlier epochs (2015.2–2016.4) as shown in Figure 1. This latest observation was timed close to a period of increased high-energy activity from the source. We show in Figure 6 our

HST photometry alongside the X-ray light curve from the Neil Gehrels Swift Observatory X-ray Telescope (XRT; built using the tools described in Evans et al. 2007, 2009), and Fermi Gamma-ray Burst Monitor (GBM; Meegan et al. 2009) trigger times¹⁴ in the vicinity of SGR 1935+2154. The HST observation for Epoch 2021.4 occurred on 2021 June 1, with one of the first bursts from the period of mid-2021 activity being reported by Fermi on June 24 (Lesage et al. 2021). As can be seen from contemporaneously scheduled Swift XRT observations, at Epoch 2021.4 the source appears to be at its quiescence level, and there had been no prior triggers. This perhaps indicates the NIR brightness changes are not correlated to changes at higher energies. Such behavior in the most recent epoch is at odds with earlier findings based on the first three epochs (Levan et al. 2018), also shown in Figure 6, where the NIR brightness state appears more closely linked to the high-energy activity. Any disconnect may indicate separate emission mechanisms for the two energy regimes, but a statistically rigorous analysis of the cohesion of multiwavelength activity requires a significant number of additional epochs of NIR monitoring—both during active and quiescent periods.

Our searches found no significant signs of variability within each epoch’s observation. A $p = 1.6\%$ rejection of the null hypothesis of no variability for the latest, and brightest, epoch does perhaps offering some marginal indication that warrants further investigation. Although short period variability in SGRs on the timescales of their magnetars’ rotation periods (seconds) have been found (e.g., Kern & Martin 2002; Dhillon et al. 2011), the origin of any minutes to hour long timescale variability would be less obvious. Additional observations while the source is brighter (which enable more precise photometry), have a better chance to rule on the presence of variability of the source over these timescales.

¹⁴ Fetched from <https://heasarc.gsfc.nasa.gov/W3Browse/fermi/fermigtrig.html>.

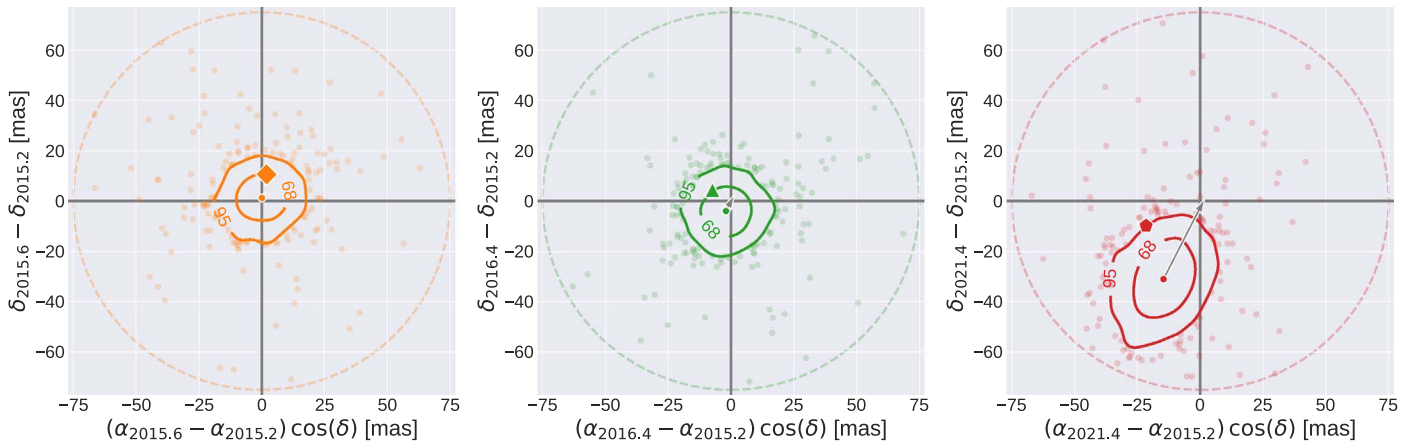


Figure 3. Equatorial offsets of sources between different HST epochs in the absolute astrometric reference frame of Gaia. Equatorial coordinates on the axes labels are denoted with a subscript indicated the epoch they refer to. In each subplot the position of SGR 1935+2154 is given by the large colored marker. Overlaid are contours of 68th and 95th percentiles ($P_{x\%}$; determined via a Gaussian kernel-density estimator), showing the distribution of offset values for all sources in the image that are close in brightness to SGR 1935+2154. Those sources outside $P_{95\%}$ are individually plotted. The peak of the distribution is marked by a small circle marker, and gray lines guide the eye to the location of zero offset. A gray vector is added to each subplot (although not visible on the left subplot), which denotes the direction and magnitude of motion expected from a model of differential Galactic rotation in the direction of SGR 1935+2154 for a source 8.5 kpc away—the distance of the Perseus arm of the Galaxy along this sight line. The large dashed ellipses mark the offset limit, based on the tolerance of source matching used (see Section 4.2).

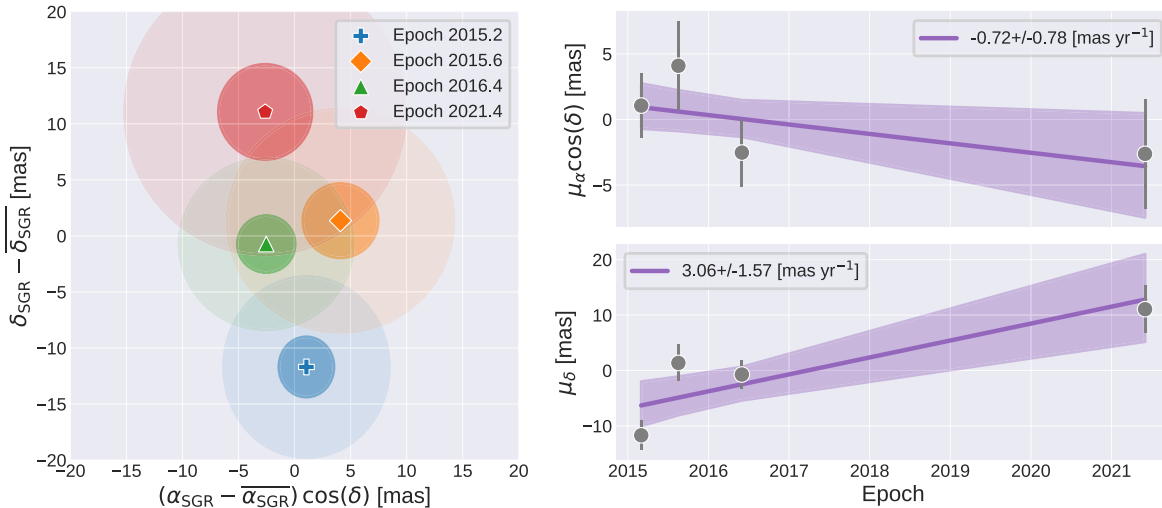


Figure 4. Left: equatorial offsets of SGR 1935+2154 in the Gaia absolute frame for our HST epochs, relative to its mean position. These offsets have been corrected for Galactic motion of SGR 1935+2154 due to differential Galactic rotation and the solar peculiar velocity, assuming a distance of 6.6 ± 0.7 kpc to the SGR. 1σ and 3σ uncertainties on the positions are given by the darker and lighter ellipses surrounding each point. Right: linear fitting to equatorial offsets of SGR 1935+2154. The uncertainties of each offset (gray markers) include contributions from the positional uncertainty on SGR 1935+2154, the offset residuals of the astrometric tie to the Gaia frame (Table 3), and the uncertainty on the Galactic motion correction. The value of fitted slope, which gives the PM constraint, is shown by the legend in each subfigure, with the shaded area indicating the 1σ uncertainty on the model.

One explanation for the origin of the NIR counterpart at the location for magnetars is emission from a debris disk (e.g., Perna et al. 2000), heated by X-ray emission from the magnetar itself. Such a disk is claimed to power the emission seen in 4U 0142 (Wang et al. 2006). The NIR emission associated with 4U 0142 shows variability at the ~ 0.5 magnitude level, comparable to SGR 1935+2154. However, in the disk scenario, the NIR is expected to vary closely in sync with changes in X-ray activity (e.g., Rea et al. 2004). This is not obviously the case with SGR 1935+2154 (Figure 6), particularly given the most recent HST epoch where the NIR emission is at its brightest during an X-ray quiescent period. Such a lack of correlation between frequency bands has been seen in magnetars with much richer NIR and X-ray data (e.g., Durant & van Kerkwijk 2006).

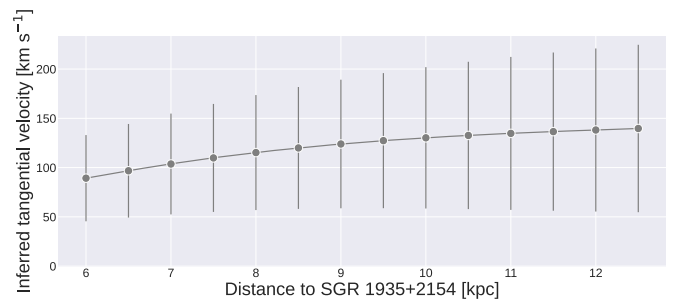


Figure 5. The inferred tangential space velocity of SGR 1935+2154 for a range of assumed values for the distance. The nonlinear variation is a result of the differential Galactic rotation model, which is used to subtract of the bulk field motion before calculating the peculiar motion of SGR 1935+2154 (Sections 3.2 and 4.2).

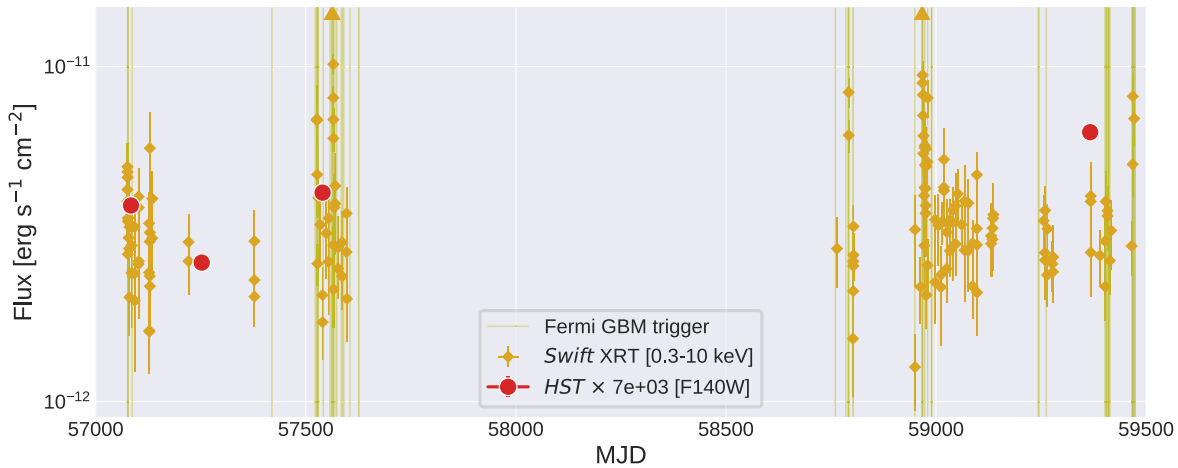


Figure 6. The light curve of SGR 1935+2154 in the NIR (HST F140W) and X-ray (Swift XRT). Overlaid at the times for Fermi GBM triggers in the vicinity. The latest HST epoch was taken during a period of relative quiescence, in terms of high-energy activity, yet is significantly (~ 0.5 to 1 mag) brighter than previous epochs. The intensive mid-late 2021 activity appears to the right of the plot in the form of a high density of Fermi GBM triggers and renewed X-ray activity. (Note for clarity, some high flux Swift XRT points have been clipped, and are indicated by upward triangles at the top of the plot.)

Although direct thermal surface emission from the magnetars cannot account for optical/NIR emission due to the unrealistic brightness temperatures inferred, an origin for the emission in the magnetosphere is a possibility. In this scenario, shearing of the magnetic field, caused by starquakes, populates a hot plasma corona surrounding the magnetar (Beloborodov & Thompson 2007, and references therein). Although models for the NIR emission are able to reproduce the observed levels of emission seen in magnetars (Zane et al. 2011), relatively little is discussed about the timescales or amplitudes of any variability. Nonetheless, for a magnetosphere origin, emission would be expected to vary roughly concurrently across bands (Tam et al. 2008).

Given the prevalence of binaries systems among massive stars (e.g., Sana et al. 2012), it is likely SGR 1935+2154 did (or does) reside in a binary. The prospects of a binary companion as the NIR emission source require the binary survived the mass loss and natal kick brought about by the supernova. However, stellar companions would be expected to be much brighter than our detection: for a roughly equal mass binary, assuming an O9V star spectrum (Pickles 1998) with $M_V = -4.49$ mag undergoing $A_V = 6.6$ – 8.8 (Green et al. 2019)¹⁵ at a distance of 6.6 ± 0.7 kpc, we might expect it to appear as an $m_{F140W} \sim 13$ – 13.5 mag source, far brighter than any current detection. A extremely low mass companion—and consequently extreme initial mass ratio binary—would need to be inferred to remain compatible with the brightness of the NIR counterpart. For this reason we disfavor a companion as the origin of the emission. A fuller discussion of magnetar binary companions, including SGR 1935+2154, is presented by Chrimes et al. (in preparation).

5.2. Implications for the Progenitor from PM

Using two methods to measure the tangential velocity of SGR 1935+2154, we obtained no strongly significant indications of motion, with a 2.1σ limit on this velocity of $\lesssim 100$ km s⁻¹. The observed velocity distribution of neutron stars (NSs), measured primarily from pulsars, is quite poorly understood, particularly so

for the presence and relative contribution of any low-velocity component (e.g., Arzoumanian et al. 2002; Brisken et al. 2003; Hobbs et al. 2005; Verbunt et al. 2017). However, even Hobbs et al. (2005), where the overall velocities are fit with a single, wide Maxwellian distribution and no low-velocity component, we find that $\sim 20\%$ of the transverse velocities of young (characteristic age < 3 Myr) are ≤ 100 km s⁻¹. Our PM constraints therefore place SGR 1935+2154 as relatively low velocity, at least compared to the overall pulsar distribution, but not exceptionally so. It is also equal to the lowest tangential velocities found for the few magnetars with such constraints. Further comparison of magnetar and pulsar kick distributions is given in Section 5.4.

There are astrophysical reasons one may expect a measure of bimodality in the velocity distribution of NSs. First, the comparative prevalence of low mass stars¹⁶ and the relatively sharp lower-mass limit cutoff at $M_{ZAMS} \simeq 8 M_\odot$ for a supernova (e.g., Smartt 2009), should result in a *pileup* of low ejecta mass events, in which the imparted supernova kick on the NSs is correspondingly small (given some relation between supernova ejecta mass and imparted kick; e.g., Bray & Eldridge 2016). The less-numerous tail of higher mass supernova progenitors, with correspondingly larger ejecta masses would then contribute to a wider, high-velocity component. Second, binary interactions will contribute to this bimodality. If the NS is borne of an supernova in a preexisting binary, the velocity will be lower than if the supernova progenitor’s binary had already been disrupted due to the previous supernova of its companion—in these cases the supernova progenitors may already have a significant velocities, increasing the mean and spread of any resultant NS velocity distribution produced from such stars. The low velocity of SGR 1935+2154 would then hint toward a lower-mass progenitor and/or it being the primary supernova in any putative binary system to which it belongs (with implications for companion emission searches—Section 5.1). We must caveat such discussion with our lack of line-of-sight information, meaning we have no constraints on the component of the velocity along this axis.

There are alternative, non-core-collapse, theoretical models to create magnetars—these typically involve mergers or accretion in systems including white dwarfs and/or NSs (Margalit et al. 2019;

¹⁵ The spread in extinction values is largely governed by whether a dust cloud at a similar distance to our adopted distance of SGR 1935+2154 is included.

¹⁶ Here, *low* is a relative term, used within the domain of stars that are able to produce a NS at their end of their lives in a supernova.

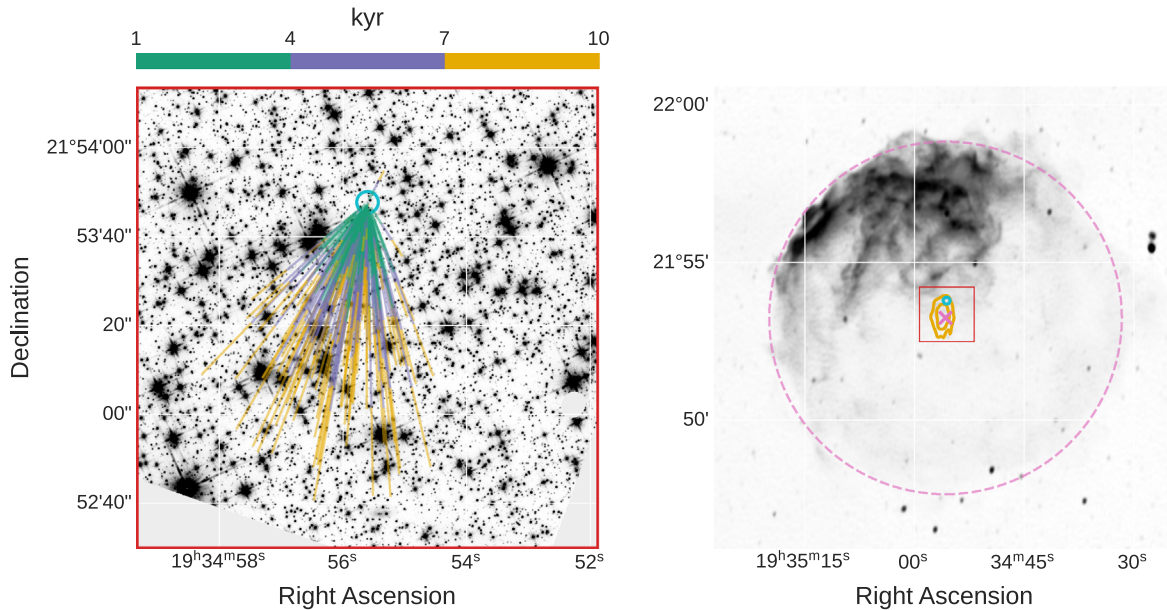


Figure 7. Left: the position and origin of SGR 1935+2154 in our Epoch 2021.4 HST WFC3/IR image. The observed location of SGR 1935+2154 is marked by the blue circle, radiating from this point are 150 realizations of our PM constraints shown as colored lines. The lines show the expected position of the SGR assuming linear motion and not accounting for the motion of the Sun. The lines are color coded to indicate ages of 1–4, 4–7 and 7–10 kyr of SGR 1935+2154, as indicated by the color bar. The low significance of the PM does allow for an origin of SGR 1935+2154 in most directions from its current position, albeit at a lower probability than a south-southeast origin. Right: a 1.28 GHz continuum image of SNR G57.2+08 from the MeerKAT telescope. The current position of SGR 1935+2154 is again indicated by a blue circle, with the contours showing the $P_{68\%}$ and $P_{95\%}$ distribution of origins for the source based on our PM constraints, assuming a 16 kyr age of the magnetar. A pink dashed circle guides the eye to the extent of SNR G57.2+08 based on the morphology of the remnant to the north. The center of this circle is indicated by the pink \times symbol. The view of the left HST panel is indicated by the red square.

Zhong & Dai 2020). Given the association to SNR G57.2+08 (see Section 5.3), we have above concentrated on implications given a core-collapse origin.

5.3. Origin and Association to SNR G57.2+08

The typically young span inferred for magnetar life-times arises from their associations with SNRs, which can be age dated (Allen & Horvath 2004), and their links to nearby clusters, which, given PM constraints for the magnetar, can provide age constraints by tracing the PM back in time to the cluster (e.g., Tendulkar et al. 2012). Such *kinematic* ages are typically more reliably than *characteristic* ages derived from the spin-down of the magnetic field, which include a number of overly simplifying assumptions about the magnetic field and its evolution (Viganò et al. 2013). Kinematic ages for magnetars are typically 10^3 – 10^4 yr.

The expected young age, and our relatively low PM value, can be used to determine that the present location of SGR 1935+2154 is close to its birthplace. To visualize this, in Figure 7 (left) we plot random realizations of our PM, tracing back typical ages of magnetars. The origin is comfortably contained within our HST imaging for typical magnetar ages.¹⁷ Searching for possible associations or clusters as the birthplace of the magnetar progenitor is, however, difficult given distance estimates to SGR 1935+2154 are significantly further than even state-of-the-art cluster searches allow (e.g., Castro-Ginard et al. 2020).

Instead, we turn our attention to the magnetar’s spatial coincidence with SNR G57.2+08 and reassess this in the light of our PM constraints. Similar analysis has been done for other

SNR-related magnetars (e.g., Tendulkar et al. 2013). We show in Figure 7 (right) the position of the magnetar alongside contoured realizations of our PM traced back 16 kyr. This nominal age is motivated by studies of the age of SNR G57.2+08 (Ranasinghe et al. 2018; Zhou et al. 2020). The contours are overlaid on a radio continuum image at 1.28 GHz from the MeerKAT telescope (Booth et al. 2009). A *by-eye*-placed dashed circle indicates the extent of SNR G57.2+08 based mainly on the bright northern lobe. When comparing the most likely origin of SGR 1935+2154 from the PM contours, we see that this matches up very well with the center of the SNR (pink cross). Thus, although SGR 1935+2154 was already highly consistent with sharing a common origin with SNR G57.2+08, the PM constraints we derive here only serve to strengthen this association by suggesting the magnetar’s birthplace (if it has an age equal to that of SNR) is almost exactly the geometric center of SNR G57.2+08.

Searching for a potential surviving unbound binary companion to the magnetar is, in principle, possible.¹⁸ However, the sheer density of sources in the field, the wide range of plausible PMs of the companion, and the lack of color information for comparably bright sources, makes drawing definitive conclusions tricky. Future characterization of the field in order to build spectral energy distributions (SEDs) for the sources and compare with binary population synthesis models may allow for a more detailed study of any surviving companion.

5.4. Comparison of Magnetar and Pulsar Kick Distributions

There are currently few published PM constraints for magnetars. To our knowledge, the six presented in Helfand et al. (2007),

¹⁷ Due to telescope orientation changes, the field of view for Epochs 2015.2 and 2015.6 are more significantly truncated along this region.

¹⁸ Assuming that the NIR counterpart emission is not coming from a bound surviving companion, which is itself a distinct possibility (Section 5.1).

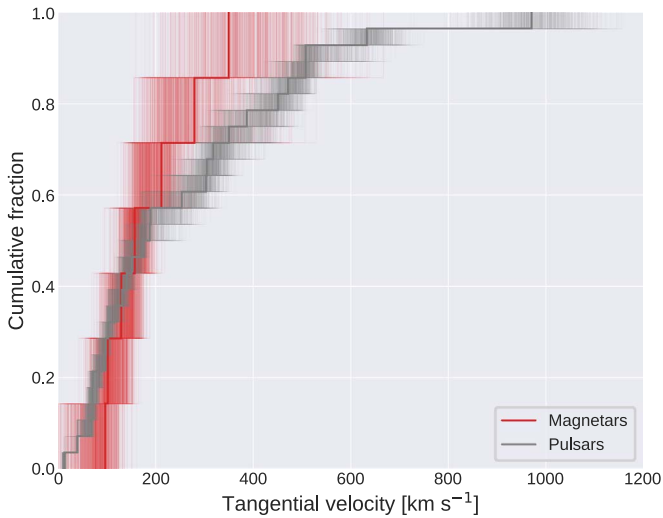


Figure 8. The cumulative distribution of tangential velocities for magnetars and pulsars. Nominal values are presented as thicker lines, with 1000 realizations of each distribution, assuming Gaussian uncertainties, plotted as fainter lines. Performing Anderson–Darling tests between these 1000 realizations gave no results with a $>2\sigma$ significance, indicating there is currently no evidence to suggest magnetar velocities are distinct from the pulsar distribution. Data for the pulsars were taken from Verbunt et al. (2017), which have here been corrected for differential Galactic rotation and peculiar solar motion using the prescription described in Section 4.2. Data for the magnetars were taken from this work and Helfand et al. (2007); Deller et al. (2012); Tendulkar et al. (2012, 2013)—these velocities were taken already corrected for Galactic rotation and solar motion, using similar models but with different values. In practice, any difference in these corrections are dwarfed by the overall uncertainty on the values.

Deller et al. (2012), Tendulkar et al. (2012), and Tendulkar et al. (2013) are here added to by SGR 1935+2154, giving a sample of seven. Adding our new value of $97 \pm 48 \text{ km s}^{-1}$ to the values in Table 7 of Tendulkar et al. (2013), we find the (mean, median, and standard deviation) of magnetar tangential velocities are approximately (190, 160, 90) km s^{-1} . In Figure 8 we show a comparison of magnetar tangential velocities to the much more numerous *young* pulsars (Verbunt et al. 2017). Given the close links between magnetars and pulsars, and even potential overlap in membership for some sources (e.g., Kaspi & McLaughlin 2005; Rea et al. 2010), we may expect their kick distributions to arise from a single distribution. Indeed, formally we found no evidence to reject this hypothesis, and conclude that they are indistinguishable, given current constraints. The lack of any high-velocity magnetars (i.e., $\nu_T \gtrsim 500 \text{ km s}^{-1}$), e.g., the pulsar distribution, is not unusual given the comparative sample sizes.

6. Summary

We have presented new HST NIR observations of SGR 1935+2154 that significantly extend the baseline of high-resolution observations for this magnetar to ~ 6 yr. Using these we have constrained the tangential velocity of the source, finding a $\sim 2.1\sigma$ detection of motion— $\nu_T = 97 \pm 48 \text{ km s}^{-1}$ —that indicates it to be moving at a modest velocity compared to the distribution of pulsar kick velocities (Verbunt et al. 2017) and other magnetars. To properly assess the statistical significance of this velocity, additional constraints are required over a longer baseline (see discussion in Section 4.2). However, our conclusions remain largely-unchanged if we consider it as a null detection, given our uncertainty on the measurement is low compared to typical magnetar velocities. The NIR brightness of

the source has now been seen to vary by one magnitude, with it being significantly brighter in the most recent epoch, despite the NIR observation being taken during a period of X-ray quiescence. There is tentative evidence of shorter timescale variability in the NIR, although additional observations while the source is brighter are needed to confirm this. The origin of the NIR emission remains unclear, although indications of a lack of correlation with X-ray behavior, if confirmed, would prove problematic for debris disk or magnetosphere models of the emission. Alternative origins, such as a binary companion, will require fuller characterization of the NIR SED in order to be properly evaluated. Even with the increase in brightness, observations in the NIR of this still faint and crowded magnetar remain solely in the remit of space-based facilities such as HST and the James Webb Space Telescope. Constraints on magnetar velocities remain sparse. With current statistics, they remain indistinguishable from the pulsar distribution.

J.D.L. wishes to thank Rolly Bedin for fruitful discussions relating to HST astrometry. J.D.L. acknowledges support from a UK Research and Innovation Future Leaders Fellowship (MR/T020784/1). A.J.L. has received funding from the European Research Council (ERC) under the European Union’s Seventh Framework Programme (FP7-2007-2013) (grant agreement No. 725246). K.W. acknowledges support through a UK Research and Innovation Future Leaders Fellowship (MR/T044136/1) awarded to Dr. B. Simmons. The MeerKAT telescope is operated by the South African Radio Astronomy Observatory (SARAO), which is a facility of the National Research Foundation, an agency of the Department of Science and Innovation. We thank B. Stappers and I. Heywood for providing us the MeerKAT image of SNR G57.2+08. Based on observations made with the NASA/ESA Hubble Space Telescope, obtained at the Space Telescope Science Institute, which is operated by the Association of Universities for Research in Astronomy, Inc., under NASA contract NAS 5-26555. These observations are associated with programs 14055, 14502, and 16505.

Facilities: HST (WFC3/IR), Swift, Fermi.

Software: Astropy (Astropy Collaboration et al. 2013, 2018), DOLPHOT (Dolphin 2016), Imfit (Newville et al. 2014), spalipy (Lyman 2021), stsynphot (Lim et al. 2021), TOPCAT (Taylor 2005), uncertainties.¹⁹

ORCID iDs

J. D. Lyman  <https://orcid.org/0000-0002-3464-0642>
 A. J. Levan  <https://orcid.org/0000-0001-7821-9369>
 K. Wiersema  <https://orcid.org/0000-0002-9133-7957>
 C. Kouveliotou  <https://orcid.org/0000-0003-1443-593X>
 A. A. Chrimes  <https://orcid.org/0000-0001-9842-6808>
 A. S. Fruchter  <https://orcid.org/0000-0002-6652-9279>

References

- Allen, M. P., & Horvath, J. E. 2004, *ApJ*, 616, 346
 Anderson, J. 2016, Empirical Models for the WFC3/IR PSF Instrument Science Report, Space Telescope Science Institute, *WFC3 2016-12*
 Arzoumanian, Z., Chernoff, D. F., & Cordes, J. M. 2002, *ApJ*, 568, 289
 Astropy Collaboration, Robitaille, T. P., Tollerud, E. J., et al. 2013, *A&A*, 558, A33
 Astropy Collaboration, Price-Whelan, A. M., Sipőcz, B. M., et al. 2018, *AJ*, 156, 123

¹⁹ <http://pythonhosted.org/uncertainties/>

- Bailes, M., Bassa, C. G., Bernardi, G., et al. 2021, *MNRAS*, **503**, 5367
- Bedin, L. R., & Fontanive, C. 2018, *MNRAS*, **481**, 5339
- Bedin, L. R., & Fontanive, C. 2020, *MNRAS*, **494**, 2068
- Beloborodov, A. M., & Thompson, C. 2007, *ApJ*, **657**, 967
- Beniamini, P., Giannios, D., & Metzger, B. D. 2017, *MNRAS*, **472**, 3058
- Bhandari, S., Heintz, K. E., Aggarwal, K., et al. 2022, *AJ*, **163**, 69
- Bochenek, C. D., Ravi, V., Belov, K. V., et al. 2020, *Natur*, **587**, 59
- Bochenek, C. D., Ravi, V., & Dong, D. 2021, *ApJL*, **907**, L31
- Booth, R. S., de Blok, W. J. G., Jonas, J. L., & Fanaroff, B. 2009, arXiv:0910.2935
- Bray, J. C., & Eldridge, J. J. 2016, *MNRAS*, **461**, 3747
- Brisken, W. F., Fruchter, A. S., Goss, W. M., Herrnstein, R. M., & Thorsett, S. E. 2003, *AJ*, **126**, 3090
- Burns, E., Svinkin, D., Hurley, K., et al. 2021, *ApJL*, **907**, L28
- Castro-Ginard, A., Jordi, C., Luri, X., et al. 2020, *A&A*, **635**, A45
- CHIME/FRB Collaboration, Andersen, B. C., Bandura, K. M., et al. 2020, *Natur*, **587**, 54
- Chrimes, A. A., Levan, A. J., Groot, P. J., Lyman, J. D., & Nelemans, G. 2021, *MNRAS*, **508**, 1929
- Deller, A. T., Camilo, F., Reynolds, J. E., & Halpern, J. P. 2012, *ApJL*, **748**, L1
- Dessart, L. 2019, *A&A*, **621**, A141
- Dhillon, V. S., Marsh, T. R., Littlefair, S. P., et al. 2011, *MNRAS*, **416**, L16
- Ding, P.-J., Zhu, Z., & Liu, J.-C. 2019, *RAA*, **19**, 068
- Dodson, R., Legge, D., Reynolds, J. E., & McCulloch, P. M. 2003, *ApJ*, **596**, 1137
- Dolphin, A. 2016, DOLPHOT: Stellar Photometry, Astronomical Source Code Library, ascl:1608.013
- Dolphin, A. E. 2000, *PASP*, **112**, 1383
- dos Anjos, R. C., Coelho, J. G., Pereira, J. P., & Catalani, F. 2021, *JCAP*, **2021**, 023
- Duncan, R. C., & Thompson, C. 1992, *ApJL*, **392**, L9
- Durant, M., & van Kerkwijk, M. H. 2006, *ApJ*, **652**, 576
- Ertl, T., Woosley, S. E., Sukhbold, T., & Janka, H. T. 2020, *ApJ*, **890**, 51
- Evans, P. A., Beardmore, A. P., Page, K. L., et al. 2007, *A&A*, **469**, 379
- Evans, P. A., Beardmore, A. P., Page, K. L., et al. 2009, *MNRAS*, **397**, 1177
- Fabircius, C., Luri, X., Arenou, F., et al. 2021, *A&A*, **649**, A5
- Fruchter, A. S., & Hook, R. N. 2002, *PASP*, **114**, 144
- Fruchter, A. S., Levan, A. J., Strolger, L., et al. 2006, *Natur*, **441**, 463
- Gaensler, B. M. 2014, GCN Circ., 16533, <https://gcn.gsfc.nasa.gov/gcn3/16533.gcn3>
- Gaia Collaboration, Brown, A. G. A., Vallenari, A., et al. 2021, *A&A*, **649**, A1
- Gavriil, F. P., Gonzalez, M. E., Gotthelf, E. V., et al. 2008, *Sci*, **319**, 1802
- Gravity Collaboration, Abuter, R., Amorim, A., et al. 2018, *A&A*, **615**, L15
- Green, G. M., Schlafly, E., Zucker, C., Speagle, J. S., & Finkbeiner, D. 2019, *ApJ*, **887**, 93
- Heintz, K. E., Prochaska, J. X., Simha, S., et al. 2020, *ApJ*, **903**, 152
- Helfand, D. J., Chatterjee, S., Brisken, W. F., et al. 2007, *ApJ*, **662**, 1198
- Hobbs, G., Lorimer, D. R., Lyne, A. G., & Kramer, M. 2005, *MNRAS*, **360**, 974
- Hurley, K., Boggs, S. E., Smith, D. M., et al. 2005, *Natur*, **434**, 1098
- Insera, C., Smartt, S. J., Jerkstrand, A., et al. 2013, *ApJ*, **770**, 128
- Kasen, D., & Bildsten, L. 2010, *ApJ*, **717**, 245
- Kaspi, V. M., & Beloborodov, A. M. 2017, *ARA&A*, **55**, 261
- Kaspi, V. M., & McLaughlin, M. A. 2005, *ApJL*, **618**, L41
- Kern, B., & Martin, C. 2002, *Natur*, **417**, 527
- Kirsten, F., Snelders, M. P., Jenkins, M., et al. 2021, *NatAs*, **5**, 414
- Kothes, R., Sun, X., Gaensler, B., & Reich, W. 2018, *ApJ*, **852**, 54
- Kouveliotou, C., Dieters, S., Strohmayer, T., et al. 1998, *Natur*, **393**, 235
- Lesage, S., Meegan, C., & Fermi GBM Team 2021, GCN Circ., 30331, <https://gcn.gsfc.nasa.gov/gcn3/30331.gcn3>
- Levan, A., Kouveliotou, C., & Fruchter, A. 2018, *ApJ*, **854**, 161
- Lim, P. L., Rendina, M., Sipocz, B., Desjardins, T., & Filippazzo, J. 2021, spacetelescope/stsynphot_refactor v1.1.0, Zenodo, doi:10.5281/zenodo.5020768
- Lindgren, L., Klioner, S. A., Hernández, J., et al. 2021, *A&A*, **649**, A2
- Lyman, J. D. 2021, spalipy: Detection-based Astronomical Image Registration, Astronomical Source Code Library v3.0.0, ascl:2103.003
- Margalit, B., Berger, E., & Metzger, B. D. 2019, *ApJ*, **886**, 110
- Mazets, E. P., Golentskii, S. V., Ilinskii, V. N., Aptekar, R. L., & Guryan, I. A. 1979, *Natur*, **282**, 587
- Meegan, C., Lichti, G., Bhat, P. N., et al. 2009, *ApJ*, **702**, 791
- Mereghetti, S., & IBAS Localization Team 2021, GCN Circ., 30395, <https://gcn.gsfc.nasa.gov/gcn3/30395.gcn3>
- Mereghetti, S., Savchenko, V., Ferrigno, C., et al. 2020, *ApJL*, **898**, L29
- Metzger, B. D., Beniamini, P., & Giannios, D. 2018, *ApJ*, **857**, 95
- Metzger, B. D., Margalit, B., Kasen, D., & Quataert, E. 2015, *MNRAS*, **454**, 3311
- Nakahira, S., Yoshida, A., Sakamoto, T., et al. 2021, GCN Circ., 30458, <https://gcn.gsfc.nasa.gov/gcn3/30458.gcn3>
- Newville, M., Stensitzki, T., Allen, D. B., & Ingargiola, A. 2014, LMFIT: Non-Linear Least-Square Minimization and Curve-Fitting for Python, 0.8.0, Zenodo, doi:10.5281/zenodo.11813
- Nimmo, K., Hessels, J. W. T., Airsten, F., et al. 2021, arXiv:2105.11446
- Olausen, S. A., & Kaspi, V. M. 2014, *ApJS*, **212**, 6
- Palmer, D. M., & Swift Team 2021, GCN Circ., 30406, <https://gcn.gsfc.nasa.gov/gcn3/30406.gcn3>
- Palmer, D. M., Barthelmy, S., Gehrels, N., et al. 2005, *Natur*, **434**, 1107
- Park, G., Koo, B. C., Gibson, S. J., et al. 2013, *ApJ*, **777**, 14
- Pavlovic, M. Z., Dobardzic, A., Vukotic, B., & Urosevic, D. 2014, *SerAJ*, **189**, 25
- Perna, R., Hernquist, L., & Narayan, R. 2000, *ApJ*, **541**, 344
- Pickles, A. J. 1998, *PASP*, **110**, 863
- Pleunis, Z., Good, D. C., Kaspi, V. M., et al. 2021, *ApJ*, **923**, 1
- Ranasinghe, S., Leahy, D. A., & Tian, W. 2018, *OPHyJ*, **4**, 1
- Rea, N., Testa, V., Israel, G. L., et al. 2004, *A&A*, **425**, L5
- Rea, N., Esposito, P., Turolla, R., et al. 2010, *Sci*, **330**, 944
- Reid, M. J., Menten, K. M., Brunthaler, A., et al. 2014, *ApJ*, **783**, 130
- Ridnaia, A., Frederiks, D., Golenetskii, S., et al. 2021, GCN Circ., 30409, <https://gcn.gsfc.nasa.gov/gcn3/30409.gcn3>
- Sana, H., de Mink, S. E., de Kotter, A., et al. 2012, *Sci*, **337**, 444
- Singh, S., & Roy, J. 2021, ATel, **14946**, 1
- Smartt, S. J. 2009, *ARA&A*, **47**, 63
- Sollerman, J., Yang, S., Perley, D., et al. 2022, *A&A*, **657**, A64
- Surnis, M. P., Joshi, B. C., Maan, Y., et al. 2016, *ApJ*, **826**, 184
- Tam, C. R., Gavriil, F. P., Dib, R., et al. 2008, *ApJ*, **677**, 503
- Taylor, M. B. 2005, in ASP Conf. Ser. 347, Astronomical Data Analysis Software and Systems XIV, ed. P. Shopbell, M. Britton, & R. Ebert (San Francisco, CA: ASP), 29
- Tendulkar, S. P., Cameron, P. B., & Kulkarni, S. R. 2012, *ApJ*, **761**, 76
- Tendulkar, S. P., Cameron, P. B., & Kulkarni, S. R. 2013, *ApJ*, **772**, 31
- Usov, V. V. 1992, *Natur*, **357**, 472
- Vallée, J. P. 2008, *AJ*, **135**, 1301
- Verbunt, F., Igoshev, A., & Cator, E. 2017, *A&A*, **608**, A57
- Viganò, D., Rea, N., Pons, J. A., et al. 2013, *MNRAS*, **434**, 123
- Wang, Z., Chakrabarty, D., & Kaplan, D. L. 2006, *Natur*, **440**, 772
- Woosley, S. E. 2010, *ApJL*, **719**, L204
- Woosley, S. E., Sukhbold, T., & Kasen, D. N. 2021, *ApJ*, **913**, 145
- Xiao, S., Huang, Y., Zhao, X. Y., et al. 2021, GCN Circ., 30400, <https://gcn.gsfc.nasa.gov/gcn3/30400.gcn3>
- Zane, S., Nobili, L., & Turolla, R. 2011, *ApSSP*, **21**, 329
- Zhang, B., & Mészáros, P. 2001, *ApJL*, **552**, L35
- Zhong, S.-Q., & Dai, Z.-G. 2020, *ApJ*, **893**, 9
- Zhong, S.-Q., Dai, Z.-G., Zhang, H.-M., & Deng, C.-M. 2020, *ApJL*, **898**, L5
- Zhou, P., Zhou, X., Chen, Y., et al. 2020, *ApJ*, **905**, 99